Nuclear Engineering and Technology 53 (2021) 3207–3216

Contents lists available at ScienceDirect

Nuclear Engineering and Technology

journal homepage: www.elsevier.com/locate/net

Original Article

CFD investigation of a JAEA 7-pin fuel assembly experiment with local blockage for SFR

Jae-Ho Jeong [a], Min-Seop Song [b, *]

[a] Department of Mechanical Engineering, Gachon University, 1342, Seongnam-daero, Sujeong-gu, Seongnam-si, Gyeonggi-do, Daejeon, Republic of Korea
[b] Department of Nuclear Engineering, Seoul National University, 1 Gwanak-ro, Gwanak-gu, Seoul, Republic of Korea

ARTICLE INFO

Article history:
Received 10 September 2020
Received in revised form
24 April 2021
Accepted 9 May 2021
Available online 24 May 2021

Keywords:
Local blockage
SFR
CFD
RANS

ABSTRACT

Three-dimensional structures of a vortical flow field and heat transfer characteristics in a partially blocked 7-pin fuel assembly mock-up of sodium-cooled fast reactor have been investigated through a numerical analysis using a commercial computational fluid dynamics code, ANSYS CFX. The simulation with the SST turbulence model agrees well with the experimental data of outlet and cladding wall temperatures. From the analysis on the limiting streamline at the wall, multi-scale vortexes developed in axial direction were found around the blockage. The vortex core has a high cladding wall temperature, and the attachment line has a low cladding wall temperature. The small-scale vortex structures significantly enhance the convective heat transfer because it increases the turbulent mixing and the turbulence kinetic energy. The large-scale vortex structures supply thermal energy near the heated cladding wall surface. It is expected that control of the vortex structures in the fuel assembly plays a significant role in the convective heat transfer enhancement. Furthermore, the blockage plate and grid spacer increase the pressure drop to about 36% compared to the bare case.
© 2021 Korean Nuclear Society, Published by Elsevier Korea LLC. This is an open access article under the CC BY-NC-ND license (http://creativecommons.org/licenses/by-nc-nd/4.0/).

1. Introduction

Owing to the depletion of fossil fuels and the growing problem of spent nuclear fuel, renewable energy has become a potential alternative energy resource. One of the significant criticisms of renewable energy is the expense and unpredictable electricity production. A Sodium-cooled Fast Reactor (SFR) system can be a rapid and decisive solution for the future energy crisis. The SFR system is one of the nuclear reactors in which recycling transuranics (TRUs) by reusing spent nuclear fuel sustain the fission chain reaction. This situation strongly motivated many research institutes and universities in Korea to initiate a prototype Gen-IV Sodium-cooled Fast Reactor (PGSFR) design project under the national nuclear R&D program.

The internal blockage in the SFR system's subassembly is essential because of a tight fuel bundle package with a high-power density. For assessing the reactor safety in the SFR, it is necessary to understand the coolant's thermal-hydraulic behaviors at the local blockage, such as the vortical structures of the separated flow field and the extent of overheating.

There are many experimental and analytical researches on the flow blockage in sodium flow. The experimental study on the flow blockage conducted at the Oak Ridge National Laboratory (ORNL) provides the subchannels' temperature distribution when the flow is blocked in the 19-pin test section's subchannels [Ref: [1]]. Using the coolant temperature distribution in the subchannels, many subchannel codes and CFD studies validate its reliability [Ref: [2,3]]. The subchannel code, MATRA-LMR-FB, which utilizes distributed resistance model, validated its capability to predict the reverse flow in the blockage area [Ref: [2]]. The CFD study on the flow blockage in 61-pin wire-wrapped fuel bundle was conducted with RANS modeling validated the methodology with the ORNL 19-pin flow blockage data [Ref: [3]]. Then, the effect of the flow blockage at the interior and edge subchannel on the maximum cladding temperature was figured out. The authors found that the blockage significantly increases the sodium temperature behind the blockages. Another CFD study on the effect of the blockage in the liquid metal reactor was carried based on ALFRED LFR demo fuel assembly geometry [Ref: [4]]. In this study, a triangular fuel bundle without wire was used for geometry to investigate the effect of the blockage on a local and global scale. The CFD study found that local clad temperature can reach 800°C within 4 s with blockage.

Those previous researches usually made their validation in

* Corresponding author.
E-mail addresses: ssrmin@snu.ac.kr, minseop.song@inl.gov (M.-S. Song).

https://doi.org/10.1016/j.net.2021.05.009
1738-5733/© 2021 Korean Nuclear Society, Published by Elsevier Korea LLC. This is an open access article under the CC BY-NC-ND license (http://creativecommons.org/licenses/by-nc-nd/4.0/).

Nomenclature

D	Rod diameter [m]
f	Friction factor [−]
P	Pressure [Pa]
U	Velocity [m/s]
ρ	sodium density [kg/m^3]
y^+	Dimensionless wall distance [−]
Subscripts	
form	Denote form loss
h	Denote hydraulic
i	Denotes inlet region of numerical analysis
skin	Denotes skin friction loss
t, T	Denotes turbulent flow region

subchannel scale. When the experimental data of local cladding temperature obtained around the blockage area is used, more detailed validation of the CFD result reduces the uncertainty of the result at the reverse flow region. The experimental study on sodium flow blockage with a 7-pin test section without wire conducted at JAEA can fill this gap [Ref: [5]]. The research provides temperature at the surface of cladding in detail. The thermal-hydraulic analysis on the 7-pin wire-wrapped fuel bundle was previously conducted to obtain the Nussetl number in the sodium flow and determined the proper turbulent Prandtl number [Ref: [6]]. This study found that SST turbulent model is appropriate for analyzing sodium flow in a wire-wrapped fuel bundle by comparing the friction factor from experimental data and CFD data. It was also found that conjugate heat transfer with sodium flow can be better predicted when the turbulent Prandtl number is set to 0.02 based on the correlations for heat transfer. The blockage simulation was previously performed in this research based on the CFD methodology without a detailed investigation of the local velocity and temperature distribution around the blockages.

In this study, three-dimensional structures of the vortical flow field and heat transfer characteristics in a partially blocked 7-pin fuel assembly mock-up of an SFR have been investigated through a numerical analysis using the commercial CFD code, ANSYS CFX. Complicated and separated flow phenomena in the 7-pin fuel assembly with the central 6 d-subchannel blockage were captured by the RANS flow simulation with the SST turbulence model, and by the vortex structure identification technique based on the critical point theory.

Table 1
Test section geometry parameters [Ref: [5]].

Geometry parameters	Test section
Number of pins	7
Pin diameter (mm)	6.5
Pin pitch (mm)	7.9
Heated length (mm)	450
Heat flux distribution	Uniform
Heat flux (kW/m^2)	660
Blockage type	Central
Thickness of blockage plate (mm)	0.5
Outer diameter of grid spacer (mm)	7.9
Height of grid spacer (mm)	5.0
Blockage location (mm)	350
Tube flat-to-flat distance (mm)	24
Blockage area fraction (%)	42
Spacing of the grid spacers (mm)	200

2. Analysis of the benchmark experiment

2.1. Test section

An experimental study of the 7-pin fuel assembly was carried out in the sodium boiling and fuel failure propagation test loops (SIENA) installed at PNC's Oarai engineering center [Ref: [5]]. The design specifications of the 7-pin fuel assembly are summarized in Table 1.

Fig. 1 and Fig. 2 show a schematic of the test section and an enlarged schematic of the blocked region by a blockage plate and spacer grid. As shown in Figs. 1 and 2, an electrically heated 7-pin bundle was centered in a hexagonal tube, with a 24 mm flat-to-flat distance inside. The heated pins were 6.5 mm in diameter, arranged in a triangular array with a pin pitch of 7.9 mm, and had a 450 mm heated length. The pitch-to-diameter ratio (P/D) was 1.22. The central 6-subchannel blockage plate was welded at a distance of 350 mm from the start of the heated section on the grid spacer's upstream side. The blockage plate area (0.63 × 10-4 m^2) and grid spacers area (0.61 × 10-4 m^2) blocked 23.6% and 22.8% of the total flow area (2.67 × 10-4 m^2), respectively.

2.2. Experimental method [Ref: [7]]

Fig. 3 shows a cross-sectional view of the pin where the wall-mounted thermocouple is located. As shown in Fig. 3, the wall's temperature is measured by 7 Chromel-Alumel thermocouples with a 0.3 mm diameter. Thermocouples are embedded in the fuel cladding of each pin. Fig. 4 shows the measurement positions. Those are located at the 0° center pin, 0° outer pin, 60° outer, and 120° outer angular positions.

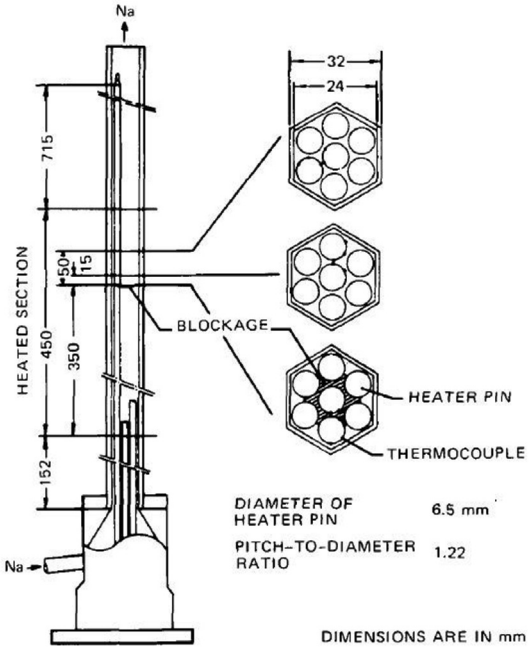

Fig. 1. Schematic of the test section [Ref: [5]].

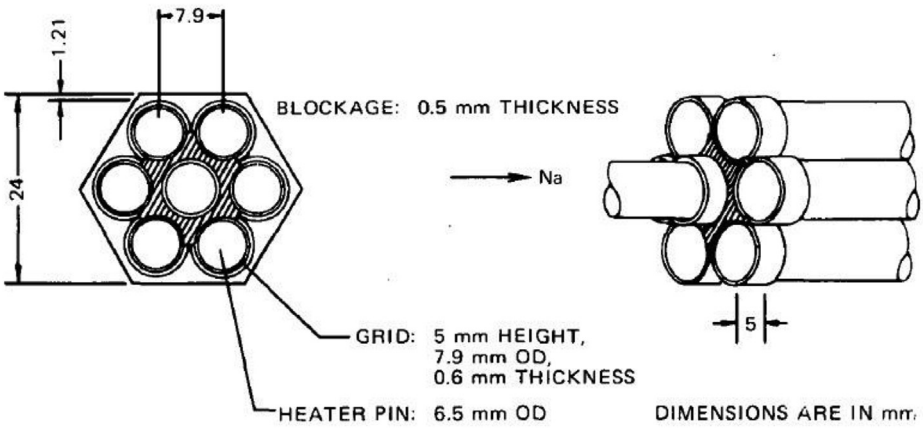

Fig. 2. Geometry of blockages [Ref: [5]].

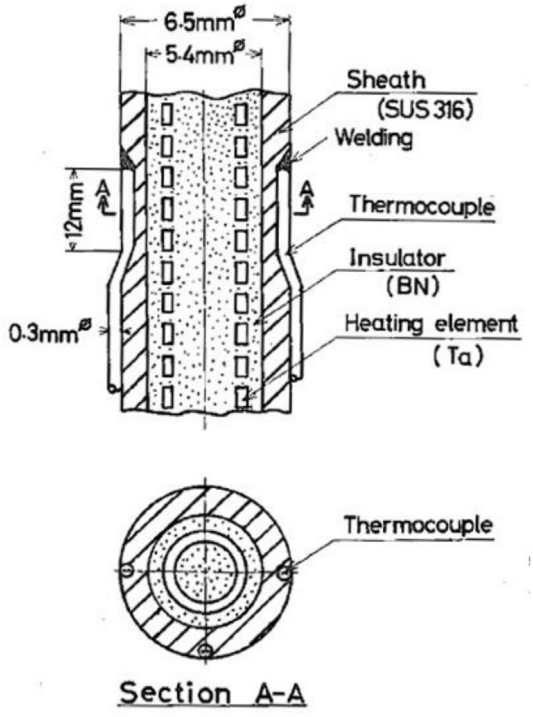

Fig. 3. Cross-sectional view of the wall surface temperature measurement region [Ref: [7]].

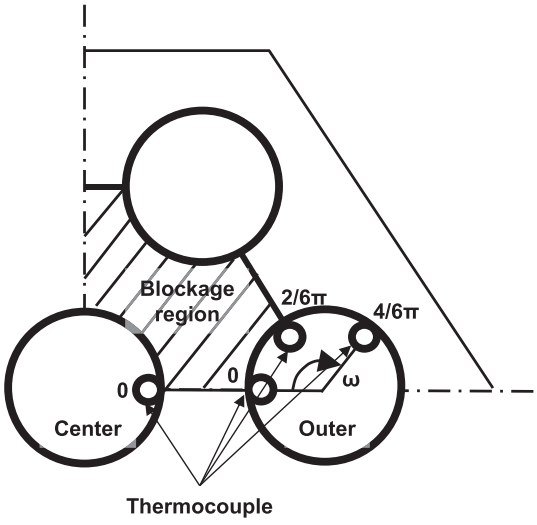

Fig. 4. Temperature measurement position of each pin [Ref: [2]].

3. Numerical analysis method

3.1. Test section of numerical analysis and computational grid system

The present CFD investigation was carried out over the full-scale experimental facility of SIENA's 7-pin fuel assembly. Fig. 5 shows the test section of the numerical analysis. Fig. 6 shows the enlarged schematic of the blockage plate and grid spacers in the 7-pin fuel assembly. As shown in Figs. 5 and 6, the test section is also composed of a heated section of 450 mm, a blockage plate with a thickness of 0.5 mm, and grid spacers with a thickness of 5.0 mm. Computational meshes are concentrated around the blockage region to capture the recirculation details, such as the wake behind the blockage plate and the grid spacers, as shown in Fig. 7. The figure represents geometry and mesh configurations around blockage plate and grid spacer. The axial length of meshes is axially 0.05 mm and 0.5 mm in the blockage plate and grid spacers, respectively. The y plus value around the rod surface was under 3.5. Total 3 cases, including bare rod case, with blockage plate, and with blockage plate and grid spacers, were studied.

The computational grid system is composed of hexahedral meshes. Table 2 describes the computational grids system. As shown in Table 2, the computational grid system is divided into two regions: a fluid and a solid part. The total number of computational grids in the system was approx. 2.78×10^6 cells [Ref: [6]].

The sensitivity on the grid (y plus, grid number) and turbulence model was conducted in the previous study that dealt with the 7 rods model and wire-wrapped rod model [6]. It was found friction factor uncertainty was under 6% for y plus change from 10 to 1, and it converged at the mesh with y plus of 2.5. The uncertainty from the turbulence model was under 3.38%.

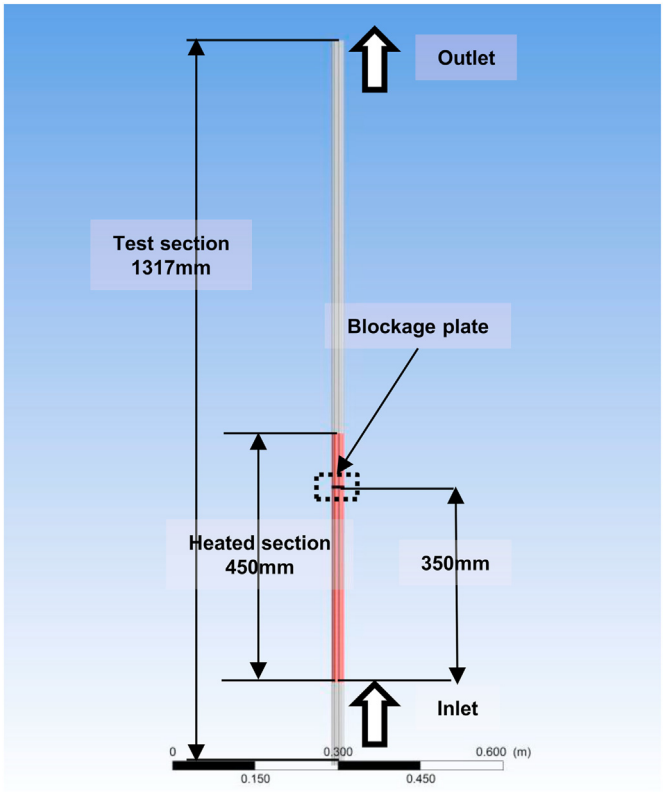

Fig. 5. Test section of numerical analysis.

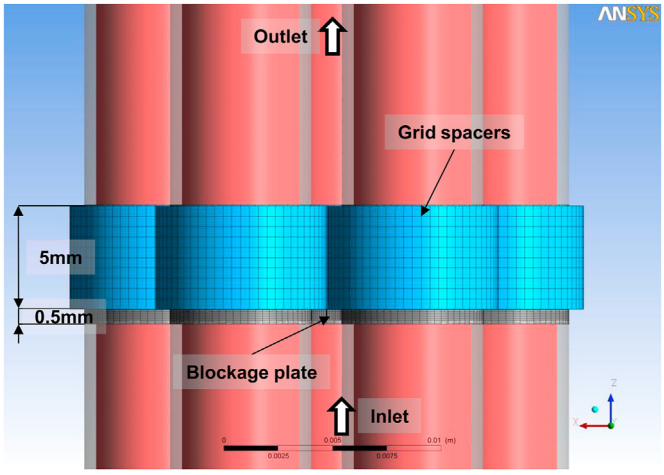

Fig. 6. Enlarged schematic of the blockage plate and grid spacers.

3.2. Computational boundary conditions

Table 3 describes the computational boundary condition of the CFD analysis. As shown in Table 3, the inlet and outlet are defined with a constant velocity of 4.92 m/s, a temperature of 556.25 K, and relative pressure of 0 Pa. The inner cladding domain of the heated section has a constant heat flux of 660 kW/m2. The outer cladding, wire, blockage plate, and grid spacers are defined with no slip condition, conservative interface flux, and smooth roughness. The duct wall is applied under no slip and adiabatic conditions. The convergence criteria for Root-Mean Square (RMS) of residuals were set 1e-8. The RMS of momentum, pressure, and energy of fluid converged under 1e-3, 1e-5, and 1e-5, respectively. The average outlet temperature converged to 578 K after 70 accumulated time steps.

3.3. Turbulence model

Numerical simulation techniques of a turbulent flow are typically divided into DNS (Direct Numerical Simulation), LES (Large Eddy Simulation), and RANS (Reynolds Averaged Navier-Stokes simulation). DNS resolves all ranges of spatial and temporal scales of the turbulence. Because the grid and time scales of the DNS need to be less than the Kolmogorov scale, which is the smallest dissipative scale, the DNS requires fine grids and a small time interval. LES solves spatially filtered Navier-Stokes equations on coarser grids. Thus, the LES does not resolve the entire scales of the turbulent flows. LES resolves only large scales of the turbulent flow. Small scales of the turbulent flow are modeled using sub-grid scale (SGS) models by Smagorinsky [Ref: [8]]. RANS solves the time-averaged Navier-Stokes equations and models all turbulence scales using turbulence models such as k-ε, k-w, and SST.

The computational cost of DNS and LES increase in cube and square for the Reynolds number compared to the case with the RANS model. Reynolds number based on the averaged axial velocity and the hydraulic diameter of the present fuel assembly is 5.92×10^4. For this reason, the DNS and LES are not feasible methods for the 7-pin fuel assembly with the local blockage. The RANS is an efficient and affordable engineering solution with good knowledge of turbulence.

The turbulence models for the RANS equations are for computing the Reynolds stresses tensor from turbulent fluctuations in the fluid momentum. Turbulence models such as k-ε, k-w, and SST have become industry-standard models and are commonly used for most types of engineering problems. However, the k-ε model has a weakness in the large adverse pressure gradients, and the k-w model is too sensitive to the inlet free-stream turbulence properties [Ref: [9]]. The SST model solves the above problems by switching to the k-ε model in the free-stream and the k-w model in the viscous sub-layer [Ref: [10]]. The minimum grid scale on the rod surface was 5.0×10^{-7} mm to capture the laminar to turbulent flow transition with SST turbulence model; the y^+ is approximately under 3.5 [Ref: [6]].

In the present study, we conducted a steady RANS simulation with the SST turbulence model for investigating the three-dimensional and vortical flow phenomena. The high-resolution scheme was used for the convective and turbulence term. The high-resolution scheme uses at least a second-wind scheme and adequate to calculate velocity variation in a narrow region with slower convergence [11]. The simulation's convergence was judged by the periodic temperature on the outlet domain of the 7-pin fuel assembly.

4. Analysis results

4.1. Comparison of CFD with experiment

Comparing the CFD analysis results with the experimental results in the 7-pin fuel assembly was carried out to validate the CFD

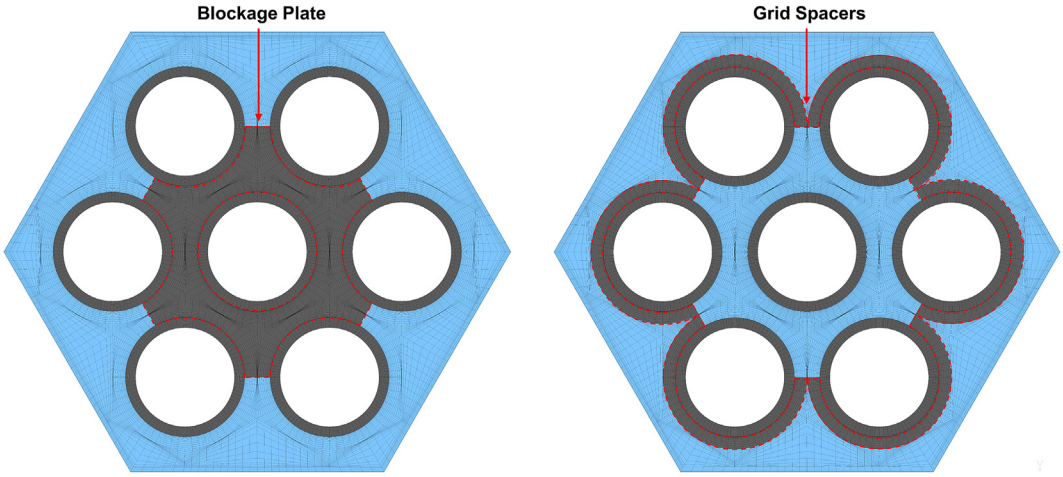

Fig. 7. Cross-section grid distribution near the blockages.

Table 2
Computational grid system.

7-Pin	Cells	Nodes	Elements
Fluids	1,583,790	1,646,330	1,583,790
Structures	1,192,100	1,341,340	1,192,100
Total	2,775,890	2,987,670	2,775,890

Table 3
Boundary condition in the 7-pin fuel assembly with blockage.

Boundary domain	Condition	Value
Inlet	- Constant velocity	4.92 [m/s]
	- Constant temperature	556.25 [K]
Outlet	- Relative pressure	0 [Pa]
Inner cladding (Heat source)	- Constant heat flux	660 [kW/m^2]
Outer cladding (=rod) and wire	- No slip	–
Blockage plate	- Conservative interface flux	
Grid spacers	- Smooth wall	
Duct Wall	- No slip	–
	- Adiabatic	
	- Smooth wall	

Table 4
Outlet temperatures of the experiment and CFD analysis results.

	Experimental results	CFD results
Outlet temperature [K]	576.40	576.45

analysis results. Table 4 shows the outlet temperatures of the experimental and CFD analysis results. As shown in Table 4, when we have the same inlet temperature, the outlet temperature difference between the experimental and CFD analysis results differs by about 1.85 K. This temperature difference can be generally induced by the reduction method of the temperature data and uncertainty of sodium property data such as density and heat capacity with temperature in CFD analysis. The temperature of the experiment is obtained by measuring some of the temperatures of the outlet region. However, the temperature of the CFD analysis is calculated using the area-averaged method.

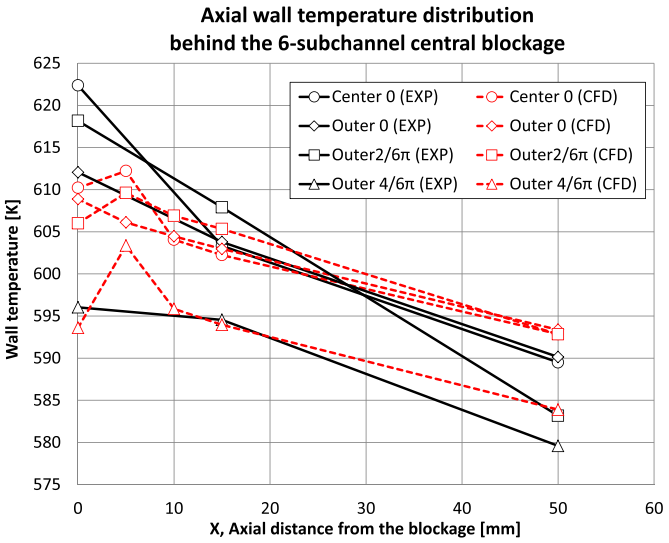

Fig. 8. Temperature comparison of experiment and numerical analysis results in the axial direction behind the 6-subchannel central blockage [Ref: [6]].

Fig. 8 shows the axial wall temperature distribution behind the 6-subchannel blockage plate [6]. The vertical axis in Fig. 8 is the wall temperature measured by the thermocouples with a 0.3 mm diameter at the 0°center pin, the 0°outer pin, the 60°outer, and 120°outer angular positions. The horizontal axis in Fig. 8 is the axial distance from the blockage location. As shown in Fig. 8, the CFD analysis results agree well with the experiment results except for the blockage region. The CFD results at measurement points decrease with the increasing distance from the blockage plate to the grid spacers. The above phenomena are related to the fact that the grid spacers also induce a partially strong blockage effect on the flow fields.

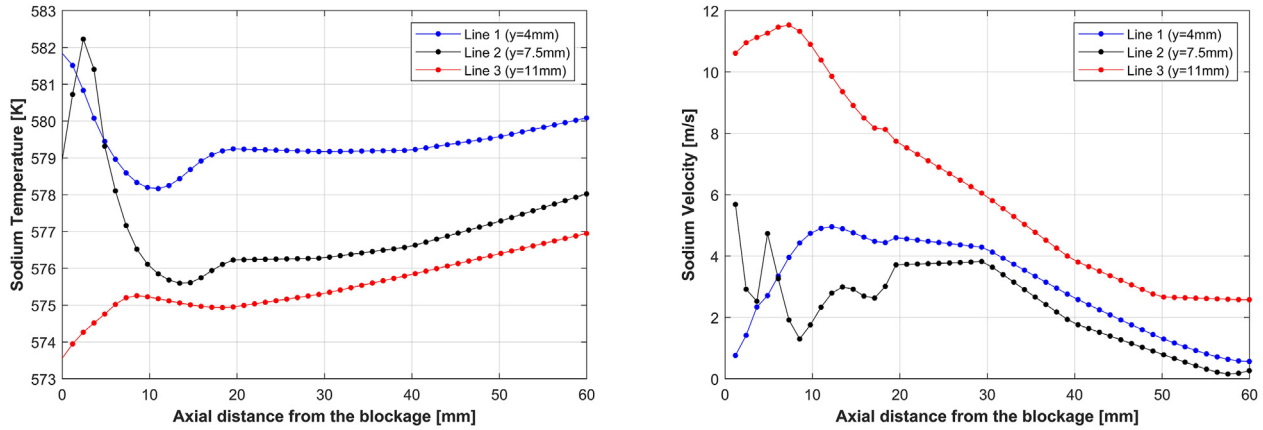

(a) Sodium Temperature Distribution (CFD)

(b) Sodium Velocity Distribution (CFD)

Fig. 9. Temperature and Velocity Distribution of Sodium behind of the blockage plate (CFD).

The change of temperature and velocity of sodium behind the blockage plate was also investigated. Fig. 9 shows a variation of those parameters at different lines. Each line started from the end of the blockage plate where z equals 0.507 m, and x is 0.0 m. As found in Fig. 8, heat transfer behind of blockage plate was disturbed behind the plates resulting in higher wall temperature. Accordingly, the higher temperature was observed in line 1 and 2. The temperature at line 3 was lower than other lines as there was no wake flow. Fig. 9 (b) clearly shows that heat removal was more efficient at line 3 than in line 1 and 2.

4.2. Three-dimensional flow field

Fig. 10 shows the axial velocity distribution in the perpendicular planes of the blockage plate downstream. Fig. 10 (a) shows the CFD analysis results with the blockage plate and grid spacers. Fig. 10 (b) shows the CFD analysis results with the blockage plate without the grid spacers. Fig. 10 (c) shows the CFD analysis results without the blockage plate and grid spacers. The wake is generally the region of recirculating flow behind the obstacle. As shown in Fig. 10 (a) and (b), both the blockage plate and the grid spacers form the wake, which has an axial velocity with a negative value. The flow blockage effect due to the wake makes the axial velocity higher than the inlet velocity. The wake with the gird spacers in Fig. 10 (a) is longer than that without the grid spacers in Fig. 10 (b). The dynamic momentum, which is proportional to the square of the axial velocity in Fig. 10 (a), is higher than that in Fig. 10 (b).

For this reason, the wake with a relatively strong recirculation in Fig. 10 (a) develops longer than the wake in Fig. 10 (b). The axial velocity partially accelerates near the outer sub-channels in the bare rod case. The X-Z plane's velocity and temperature distribution for the case with blockage plate and grid spacers were added in Fig. 11 to show how far the blockage and grid spacer affect the fluid. This figure shows the distribution of parameters at the X-Z plane with y equals 0, 0.004, 0.0075, and 0.011 m. The wake flow made behind of plate considerably reduced the velocity magnitude. The reduction of velocity was maintained by more than 25 thickness of grid spacers. The range of large wake structures behind the plate in (b) and (f) proves that the area of influence is the same.

A limiting streamline analysis based on the critical-point theory was carried out to investigate the complex vortex structures [12]. A vortex structure is elucidated from the limiting streamline on the surface based on the critical-point theory. The critical point theory shows how to understand vortex structures from the limiting streamlines. It is advantageous to observe a separated vortex near a wall. The separation line is observed at the start of vortex formation, showing discontinuity. The attachment line is made behind the separation line, indicating that the vortex is attached to the wall. A detailed explanation of the relation between vortex shape and limiting streamline can be found in the literature [12].

Fig. 12 shows the limiting streamline on the wall surface and the turbulence kinetic energy distribution on the axial direction's cross-sectional planes. Fig. 12 (a), (b), and (c) of each analysis object is the same as in Fig. 10 (a), (b), and (c). The vortical flow field in Fig. 12 (a) is far more complicated than that in Fig. 12 (b) and (c). As shown in Figs. 10 (a) and Fig. 12 (a), a boundary layer is axially developing along with the rod bundle. The boundary layer is then separated behind the blockage plate and the grid spacers. These are small-scale vortex that has length scale corresponds to blockage thickness. The locally separated vortex on the grid spacer's wall surface in the outer sub-channel starts to be formed at 10–20% of grid spacers' thickness. The separated vortex on the grid spacer's wall surface attaches at 30%–90% of the thickness. The truncated section of the end of the grid spacer generates wake vortex is attached at the downstream of 50% of a wake vortex. A large-scale vortex, which has a length scale close to rod radius, is generated by the blockage plate in Fig. 12 (a) and (b). Those vortexes have a vortex core around the plane of 518 mm. Comparing Fig. 12 (a) with Fig. 12 (b), the small-scale and large-scale vortex generated by the grid spacers and the blockage plate in Fig. 12 (a) has higher turbulence kinetic energy than that in Fig. 12 (b). Generally, the pressure loss is caused mainly by the dissipation of the turbulence kinetic energy into heat. Based on the analysis of a three-dimensional flow field, it is expected that the pressure loss caused by the large-scale vortex behavior of Fig. 12 (a) is larger than that of Fig. 12 (b).

4.3. Pressure drop characteristics

The pressure loss is generally divided into a skin-friction and

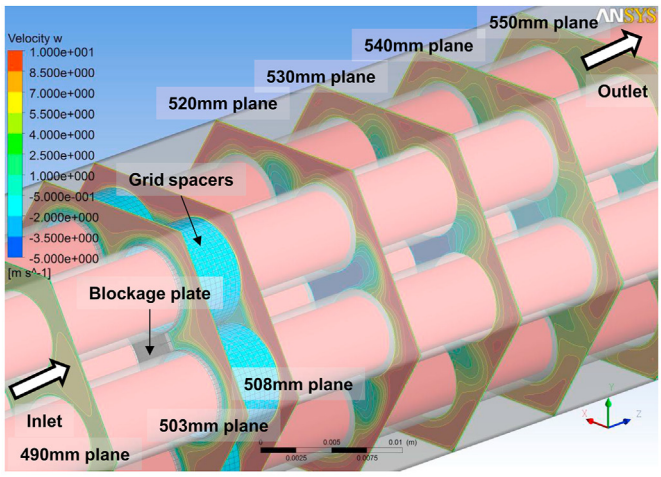

(a) With blockage plate and grid spacers

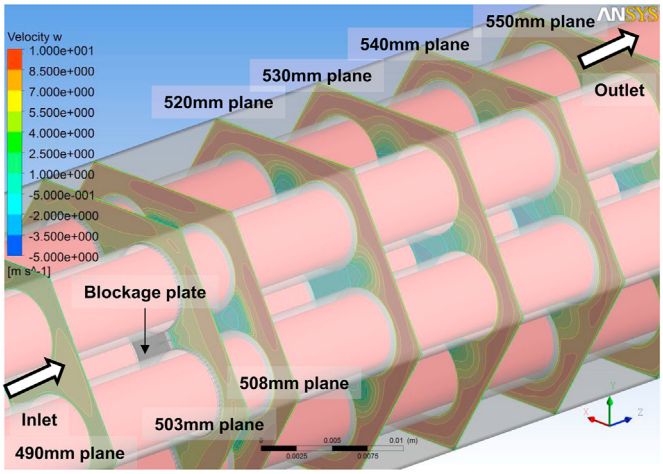

(b) With blockage plate and without grid spacers

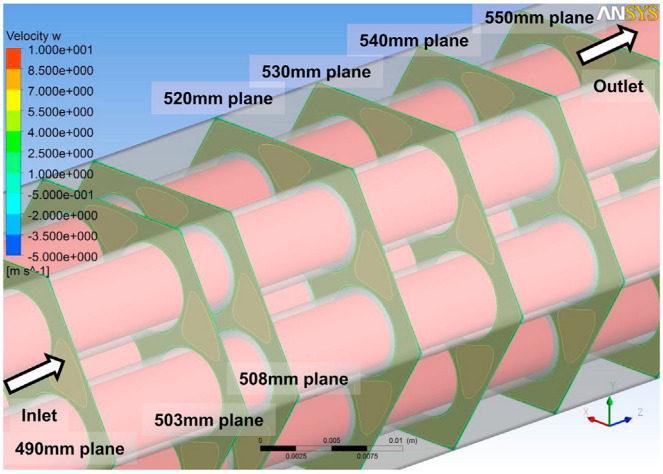

(c) Without blockage plate and grids spacers

Fig. 10. Axial velocity distribution on the cross-sectional planes perpendicular to the axial direction.

form-friction pressure drop in an internal flow. The skin-friction is due to the roughness of the fuel assembly's inner part, and the form-friction is due to obstructions such as the blockage plate and grid spacers in the fuel assembly. The friction factor from total pressure drop in the fuel assembly is calculated using the following formula.

$$f = \Delta P \times \left(\frac{D_h}{L}\right) \Big/ \left(\frac{\rho U_i^2}{2}\right) \quad (1)$$

where all various symbols are defined in the nomenclature section of this paper.

Table 5 shows that the CFD analysis calculates the friction factors. There are three different kinds of CFD analysis results to understand the dominant source generating the pressure drop. As shown in Table 5, the fuel assembly with both the blockage plate and grid spacers has the largest friction factor, which is 36% higher than that of bare rod case. The fuel assembly's friction factor with only a blockage plate is smaller than that with both and larger than that without both. The blockage plate increases friction factor about 12% compared to bare rod case. Additional friction was made by increased wall area and vortex formation.

4.4. Heat transfer characteristics

To understand the details of heat transfer characteristics in the thermal wake region, the Nusselt number was evaluated based on the CFD analysis results. In the CFD studies, the determination of the turbulent Prandtl number is essential to obtain accurate temperature filed in the fluid. In the previous study on thermal-hydraulics in 7-pin wire-wrapped fuel bundle, it was found that the prediction of the Nusselt number in sodium flow shows good agreement with the existing correlations when the turbulent Prandtl number is 0.02 [Ref: [6]]. For the Peclet number in SFR, where it ranges from 150 to 300, the Nusselt number predicted in CFD study for 7-pin with wire and without wire (bare rod) agreed well with the result with correlations of Mikityuk, Graber and Rieger, Borishanski, and subbotin [Ref: [13–16]]. Therefore, the Nusselt number calculated in this geometry would be reliable for this physics and geometry.

Fig. 13 shows the axial Nusselt number distribution around the 6-subchannel central blockage. The vertical axis in Fig. 13 is the Nusselt number calculated by the length-averaged wall surface temperature and the area-averaged bulk temperature on the cross-sectional plane at the axial position from blockage. The Nusselt number of the bare rod case is larger than the Nusselt number of other cases. It is because the heat transfer is lowered by the wakes that occur behind the blockage plate. The *Nu* number from correlations gave values ranged from 4 to 10 at this Peclet number of 230 [[6]]. The *Nu* value distribution of bare rod case fall in this range. As shown in Fig. 13, the Nusselt number dramatically decreases at the 5 mm blockage downstream. Going toward the blockage downstream, the Nusselt number continues increasing. Compared with the Nusselt number with only a blockage plate, the Nusselt number with the blockage plate and grid spacers is remarkably increasing behind the blockage region. It explains why the grid spacers just behind the blockage plate generate small-scale vortex structures with high turbulence kinetic energy. As these vortex structures go on downstream and are mixed with the flow of the outer subchannels shown in Fig. 12 (a), the heat transfer characteristics are enhanced.

Fig. 14 shows the temperature distribution and limiting streamline on the wall surface. As shown in Fig. 14 (a), (b), and (c), the temperature distribution on the wall surface is closely related to the limiting streamline on the wall surface. Based on the critical point theory, the limiting streamline with the vortex core has the highest cladding wall temperature. The limiting streamline with

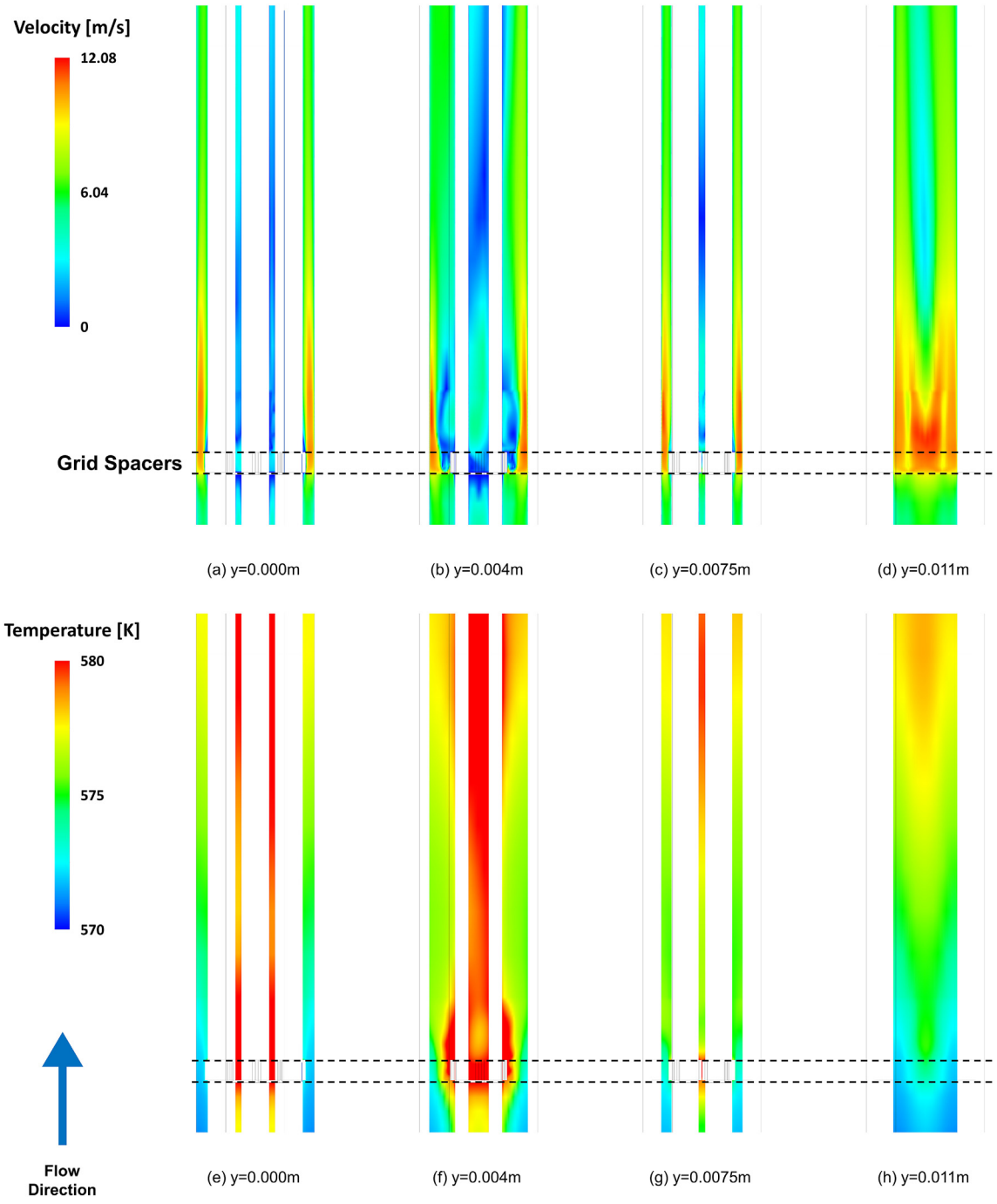

Fig. 11. Axial distribution of velocity and temperature at X-Z planes.

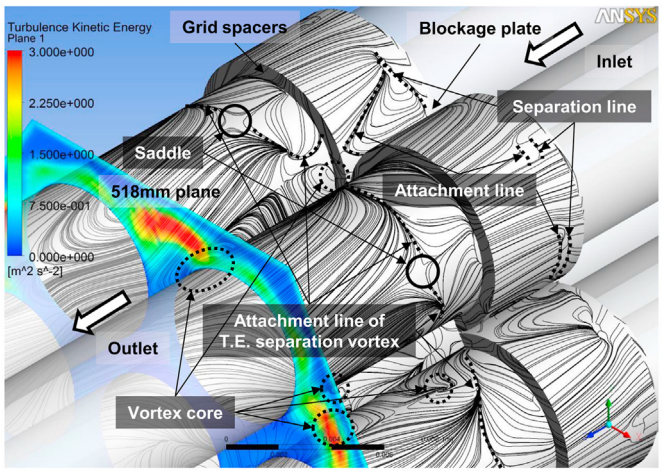

(a) With blockage plate and grid spacers

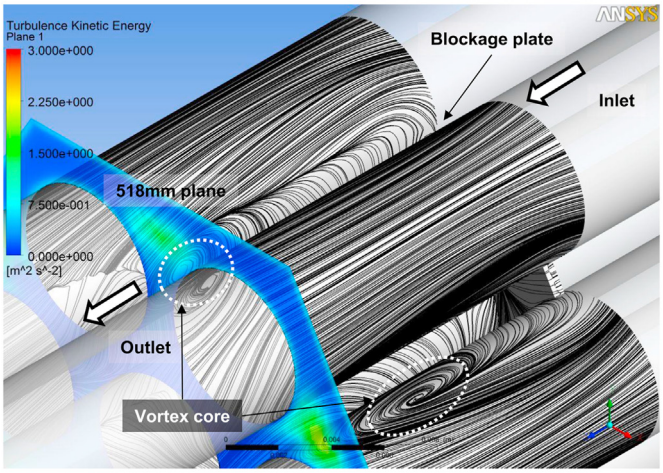

(b) With blockage plate and without grid spacers

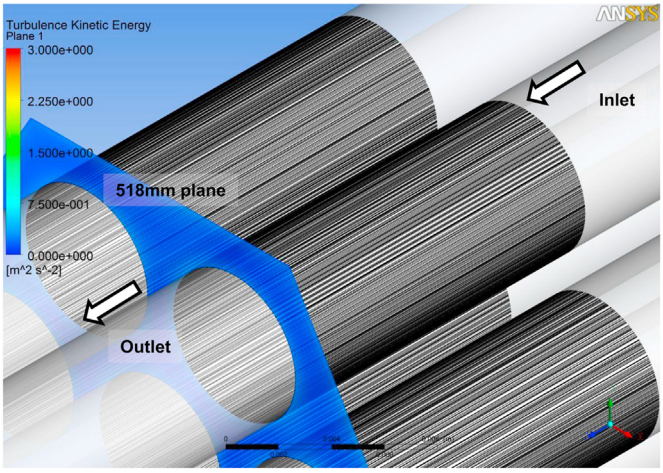

(c) Without blockage plate and grids spacers

Fig. 12. Limiting streamline on the wall surface and turbulence kinetic energy distribution on the cross-sectional planes.

the attachment line has a low cladding wall temperature. As previously mentioned, the limiting streamline is formed by the vortex structure behavior. The large-scale vortex structures supply the

Table 5
Friction factor in the 7-pin fuel assemblies.

Cases (Re = 5.92 × 10^4)	Friction factor [−]
With blockage plate (Blockage area = 0.63*$10^{-4}$$m^2$)	0.03214
With grid spacers (Blockage area = 0.61*$10^{-4}$$m^2$)	
With blockage plate	0.02646
Without grid spacers	
Without blockage plate	0.02357
Without grid spacers	

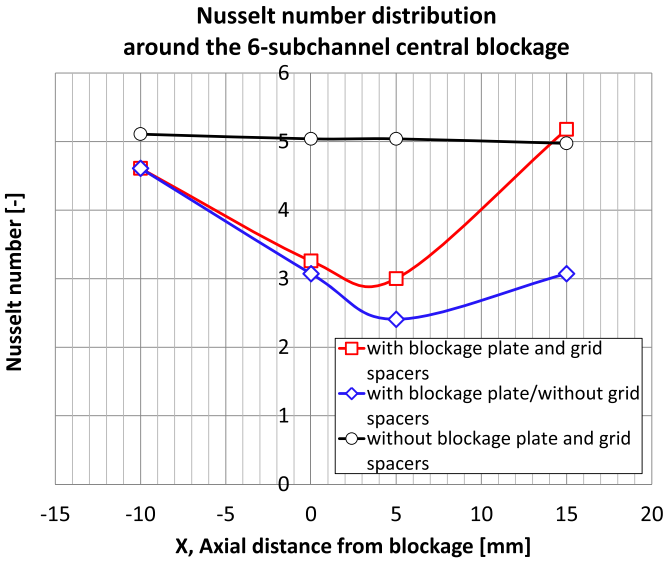

Fig. 13. Axial Nusselt number distribution around the central blockage.

thermal energy near the heated cladding wall surface downstream to the blockage plate upstream. For this region, the cladding wall surface temperature near the blockage plate and grid spacer are higher than that of the other axial positions. The vortex structure behavior significantly dominates the heat transfer characteristics.

5. Conclusions

Three-dimensional structures of a vortical flow field and heat transfer characteristics in a partially blocked 7-pin fuel assembly mock-up of an SFR have been investigated through a numerical analysis using a commercial CFD code, CFX. A RANS flow simulation with the SST turbulence model captured complicated and separated flow phenomena in the 7-pin fuel assembly with a central 6-subchannel blockage. The vortex structures are investigated using limiting streamlines. The conclusions are as below:

1. Three-dimensional multi-scale vortex structures start to be formed around the central blockage plate and grid spacer and develop in the axial direction.
2. Large-scale vortex structures and small-scale vortex structures, which are respectively generated by the blockage plate and grid spacer, dominate the heat transfer characteristics. Compared to the CFD results without a grid spacer, the grid spacer's small-scale vortex structures significantly enhance the convective heat transfer. The small-scale vortex structures tend to accelerate turbulent mixing and make the turbulence kinetic energy increase.

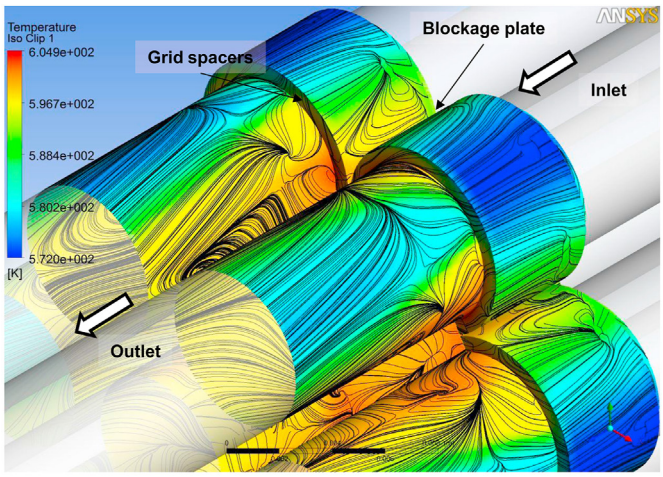

(a) With blockage plate and grid spacers

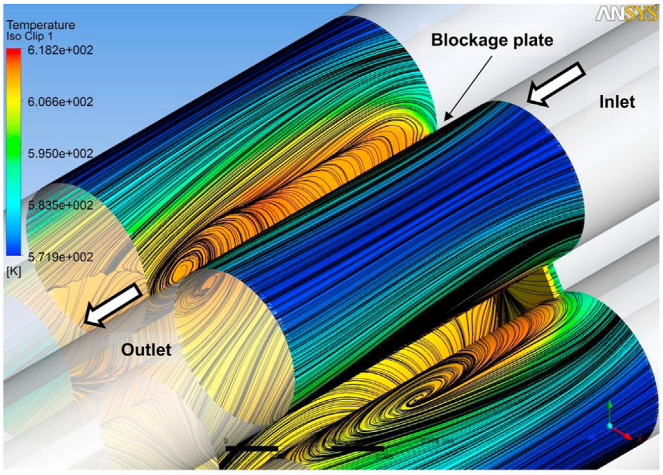

(b) With blockage plate and without grid spacers

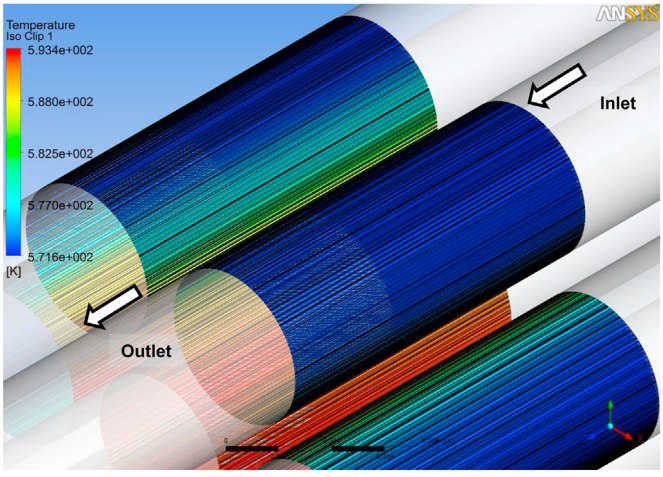

(c) Without blockage plate and grids spacers

Fig. 14. Limiting streamline on the wall surface and temperature distribution.

3. The friction factor was increase about 36% for the case with blockage plate and grid spacer, and 12% for the case with blockage plate. The increased wall area and formation of vortex increased the pressure drop.

Declaration of Competing Interest

The authors declare that they have no known competing financial interests or personal relationships that could have appeared to influence the work reported in this paper.

Acknowledgments

The research paper is made possible through the encouragement and support from Dr. Hiroyuki Ohshima of JAEA. This study has been supported by National R&D Program through the National Research Foundation of Korea funded by the Ministry of Science, ICT & Future Planning (No.2020R1G1A1099560). This work was also supported by the Gachon University research fund of 2019 (GCU-2019-0797).

References

[1] J.T. Han, Blockages in LMFBR Fuel Assemblies: a Review of Experimental and Theoretical Studies. No. ORNL/TM-5839, Oak Ridge National Lab., TN (USA), 1977.
[2] Hae-Yong Jeong, et al., Modeling of flow blockage in a liquid metal-cooled reactor subassembly with a subchannel analysis code, Nuclear technology 149 (1) (2005) 71–87.
[3] Xiang Chai, et al., Numerical investigation of flow blockage accident in SFR fuel assembly, Nucl. Eng. Des. 359 (2020) 110437.
[4] Di Piazza Ivan, et al., A CFD analysis of flow blockage phenomena in ALFRED LFR demo fuel assembly, Nucl. Eng. Des. 276 (2014) 202–215.
[5] Y. Daigo, K. Haga, A. Ohtsubo, Y. Kikuchi, Local Temperature Rise Due to a 6-Channel Blockage in a 7-Pin Bundle, JAPFNR-202, 1975.
[6] Jae-Ho Jeong, Min-Seop Song, Kwi-Lim Lee, Thermal-hydraulic effect of wire spacer in a wire-wrapped fuel bundles for SFR, Nucl. Eng. Des. 320 (2017) 28–43.
[7] K. Haga, Y. Daigo, Y. Kikuchi, A. Otsubo, The Effects of Bowing Distortions on Heat Transfer in a Seven-Pin Bundle, ASME Winter Annual Meeting, New York, NY, 1974.
[8] J. Smagorinsky, General circulation experiments with the primitive equations. I. The basic experiment, Mon. Weather Rev. 91 (1963) 99–165.
[9] D.C. Wilcox, Re-assessment of the scale-determining equation for advanced turbulence models, AIAA J. 26 (11) (1988) 1299–1310.
[10] F.R. Menter, Two-equation eddy-viscosity turbulence models for engineering applications, AIAA J. 32 (8) (1994) 1598–1605.
[11] Bran van Leer, Upwind and high-resolution methods for compressible flow, 16th AIAA Computational Fluid Dynamics Conference (2003).
[12] A.E. Perry, M.S. Chong, A description of eddying motions and flow patterns using critical-point concepts, Annu. Rev. Fluid Mech. 19 (1987) 125–155.
[13] Konstantin Mikityuk, Heat transfer to liquid metal: review of data and correlations for tube bundles, Nucl. Eng. Des. 239 (4) (2009) 680–687.
[14] H. Graeber, M. Rieger, O.E. Dwyer, Experimental Study of Heat Transfer to Liquid Metals Flowing In-Line through Tube Bundles, EURATOM, Ispra, Italy, 1973.
[15] V.M. Borishanskii, M.A. Gotovskii, E.V. Firsova, Heat transfer to liquid metals in longitudinally wetted bundles of rods, Sov. Atom. Energy 27 (6) (1969) 1347–1350.
[16] V.I. Subbotin, et al., Heat transfer in elements of reactors with a liquid metal coolant, Proceedings of the 3rd International Conference on Peaceful Use of Nuclear Energy 8 (1965).